Engineering Science and Technology, an International Journal 50 (2024) 101606

Contents lists available at ScienceDirect

Engineering Science and Technology, an International Journal

journal homepage: www.elsevier.com/locate/jestch

Enhancing formability of Ti-6Al-4V cylindrical cups by pulsating hydroforming process: Experimental, numerical and microstructural investigations

Osman Öztürk [a], Mevlüt Aydın [a], Ömer Faruk Gökcepınar [a], Harun Mert İlbeyli [b], Habip Gökay Korkmaz [c], Yusuf Furkan Yapan [d], Murat Dilmeç [e], Hüseyin Selçuk Halkacı [a], Hasan Kotan [f], Haydar Livatyalı [g], Serkan Toros [c], Mevlüt Türköz [a,*]

[a] Department of Mechanical Engineering, Konya Technical University, Konya 42250, Türkiye
[b] Department of Mechanical Engineering, Balıkesir University, Balıkesir 10145, Türkiye
[c] Department of Mechanical Engineering, Niğde Ömer Halisdemir University, Niğde 51240, Türkiye
[d] Department of Mechanical Engineering, Yıldız Technical University, İstanbul 34349, Türkiye
[e] Department of Mechanical Engineering, Necmettin Erbakan University, Konya 42090, Türkiye
[f] Department of Metallurgical and Materials Engineering, Bursa Technical University, Bursa 16310, Türkiye
[g] Department of Mechatronics Engineering, Yıldız Technical University, İstanbul 34349, Türkiye

ARTICLE INFO

Keywords:
Pulsating Hydroforming
Ti-6Al-4V
Formability
Microstructural characterization
Sheet metal forming

ABSTRACT

Ti-6Al-4V alloy sheet is an engineering material that is widely used due to its superior properties such as high strength-to-density ratio besides high temperature and corrosion resistance. However, its low formability at room temperature limits its wider applications. In this study, a cylindrical cup was hydroformed using a female die to examine how the pulsating effect would result under frictional conditions. Initially, finite element simulations were performed to design a proper die geometry. Next, forming tests were run on Ti-6Al-4V blanks under pressure increased monotonically and with pulsation, and microstructural analyses were performed on the formed specimens. The effects of pulsation frequency, amplitude, and base pressure on the formability were investigated. The nose radius/thickness ratio, maximum thinning, bursting pressure, and die-filling ratio measured on the specimens formed under monotonic and pulsating loadings were compared, and the improvement in the formability was demonstrated. An increase of 38.5 % in bursting pressure occurred and the nose radius of the part was decreased up to 30 % with pulsating loading. The die-filling ratio was improved from 87.9 % to 95.3 % with optimized pulsation parameters. The underlying microstructural reasons for the improved formability were elaborated using XRD, SEM, and TEM analyses.

1. Introduction

One of the most widely used titanium alloys is Ti–6Al-4V due to its superior properties such as high strength-to-density ratio and corrosion resistance, especially in the aerospace industry [1,2]. However, the formability of Ti–6Al-4V sheet is limited at room temperature due to low strain hardening and maximum elongation under tension [3]. Research performed to improve the formability of the Ti-6Al-4V sheet shows that superplastic forming, which is a hot forming method, raises the % elongation values. However, high energy consumption, tool damage at high temperatures, limited productivity, oxidation of the material surface, reduced fatigue life, and high forming costs are considered the drawbacks of hot forming [4–6]. Therefore, new and novel methods are required to increase the formability of Ti–6Al-4V at room temperature and the use of pulsation is the key motivation of this research.

Sheet hydroforming is not commonly used in mass production because of the low yield and high costs; however, it is preferable in special cases that need higher sheet metal formability [7]. Sheet hydroforming is generally classified into two groups; forming with a punch (SHF-P) and with a (female) die (SHF-D) [8]. In the SHF-D process, the hydraulic fluid acts as a punch without friction and the die enforces the final geometry under friction. With a lack of friction on the

* Corresponding author.
E-mail address: mturkoz@ktun.edu.tr (M. Türköz).

https://doi.org/10.1016/j.jestch.2023.101606
Received 6 October 2023; Received in revised form 14 December 2023; Accepted 30 December 2023
Available online 14 January 2024

pressurized side, local strains are more homogeneous, while the sheet material conforms to the shape of the die better. Therefore, more durable and complex-shaped sheet metal parts can be produced with SHF-D [9,10]. For example, Dilmeç et al. [11] determined the limiting drawing ratio of SS 304 by using the SHF-D process. They reported that shallow sheet metal parts can be manufactured robustly without the need to optimize the pressure and blank holder force profiles. It should also be stated that the SHF-D is different from hydraulic bulging where no die surface shapes the sheet, and thus forming is achieved by the hydraulic pressure only

Reported investigations on pulsating hydroforming mostly focus on tube forming and the work on sheet forming is limited. Mori et al. [12] conducted the first experimental studies on pulsating hydroforming. They reported that the defects, such as wrinkling due to low pressure and bursting due to high pressure, were avoided by the proposed pulsating regime in low pressure. Hama et al. and Loh-Mousavi et al. supported these experimental studies with numerical modeling and simulations [13,14]. Accordingly, wrinkling and early bursting were eliminated and a more homogeneous thickness distribution was obtained. Some researchers indicated that the pulsation of the blank-holder is also effective in improving the limiting drawing ratio by 11.53 % in hydroforming [15]. In a recent study conducted at 700 °C, pulsating tube-hydroforming was found to improve the maximum gap and the springback with a homogenous thickness distribution for spiral tube geometry [16].

Although there are many studies on pulsating tube hydroforming, studies on pulsating sheet hydroforming are very limited. For example, Yang et al. [17] investigated the effects of frequency and amplitude on the maximum bulge height of AZ31B magnesium alloy using numerical methods and reported a more uniform thickness distribution. Additionally, Hu and Pan [18] investigated the forming of AZ31 magnesium sheets by monotonic and pulsating loadings under the same maximum liquid pressure. They reported an increase in bulge height and more uniform wall thickness by pulsating loading.

The authors of the present study also investigated the effect of pulsating loading on the mechanical properties of Ti-6Al-4V alloy by using the bulge test [19] and determined the underlying microstructural phenomenon of the improved formability [20]. These studies are far from providing information about the manufacturability of parts with more complex geometries produced under the influence of friction with pulsating loading, and in the studies, only the effect of pulsating loading on the mechanical properties of the material was investigated by the bulge test, which gives the flow curves of the materials, as in the tensile test. In this context, they reported that the pulsation forming enabled a greater thickness reduction and a slightly more uniform thickness distribution when compared to monotonic loading. It was also determined that pulsation forming induced a delay in the fracture, resulting in a 15.4 % increase in the dome height, a 17 % rise in the burst pressure, and a 47 % enhancement in the formability. This increased formability was attributed to the stress relaxation that took place during the pulsating bulge test. That is, reduced dislocation density during the early stages of formation prevented dislocations from locking and postponed the fracture, resulting in enhanced dome height.

In the current study, different from our previously reported ones [19,20] and the literature, the effect of pulsating pressure was investigated for the SHF-D process applied on Ti-6Al-4V sheets using a small-scale cylindrical die. Thus, the effect of pulsating loading was investigated for small (nose) radius cups like industrial parts under frictional effects. In this context, the effects of base pressure, pulse amplitude, and frequency on the bursting pressure, nose radius/thickness ratio (R/t), die-filling ratio, and thickness strain were measured. Additionally, microstructural characterizations were performed using XRD, SEM, and TEM on the specimens before and after the forming processes.

2. Experimental details

The chemical composition of the Ti-6Al-4V alloy received in cold-rolled form is given in Table 1. Uniaxial tensile tests of the samples prepared following the ASTM E8 standard with a gauge length of 50 mm in three planer directions (0°, 45°, and 90°) were conducted three times at a speed of 25 mm/min on a Shimadzu Autograph 100 kN tensile device, and the average of the results was presented in Fig. 1. In this study, the experimental setup containing a die set, a pressure intensifier, a high-pressure line, and members were designed, manufactured and assembled for the pulsating SHF–D. A set of Finite Element (FE) simulations was conducted to determine the proper die dimensions. Monotonic and pulsating SHF-D experiments were conducted according to Taguchi L9 experimental design. Geometric dimensions and thickness distributions of all the formed specimens were measured. The microstructural analyses were performed using X-ray diffraction (XRD), field emission scanning electron microscope (FESEM), and transmission electron microscopy (TEM).

To reveal the effect of pulsating pressure in sheet hydroforming, and to increase formability and part quality, cups were formed in a cylindrical die. The nose radius of the cup was considered the measure of the formability. The as-received thickness of the Ti-6Al-4V sheet was 0.55 mm and the circular blanks were cut to 72 mm diameter. The lower die was designed with a 40 mm inner diameter, 50 mm depth, and 5 mm die shoulder (entrance) radius as seen in Fig. 2. The depth of the lower die was set to 13 mm by circular shims at the bottom so that the bottom radius was practically zero for all experiments. A self-aligning tapered roller bearing was placed under the lower die to enable a homogeneous blank holder force distribution on the specimen while the lower die was closing upwards.

The maximum pressure required to form the specimen with desired radii was calculated from the simulations at approximately 200 MPa. Thus, high-pressure hydraulic components that can withstand these pressures are needed in the transmission of pressurized liquid from the pressure intensifier to the upper die. These elements are the nipples, high-pressure tubes, the distributor (X block), the glands, the high-pressure sensor, the check valve, and the water charge tank to fill the water inside the pressure intensifier. The high-pressure circuit diagram and the assembly of the high-pressure circuit to the experimental setup are shown in Fig. 3.

Hydraulic base pressure, pulse amplitude (a), and frequency (f) were determined as the pulsation parameters. Thanks to a hydraulic unit with servo valves and a closed-loop numerical control electronic card, the pressure intensifier can be operated precisely at the desired frequency and amplitude. An example of a loading profile is given in Fig. 4.

Frequency and amplitude levels were set based on preliminary performance tests of the pressure intensifier. High amplitudes could not be obtained when the frequency was higher than 3 Hz. The maximum applicable amplitude was 10.0 MPa at 3 Hz. The lowest amplitude value was selected as 2.5 MPa because at lower amplitudes the pressure intensifier cannot provide the desired amplitude level. To summarize, a pressure range of 2.5–10.0 MPa was chosen for amplitude and 1–3 Hz for frequency. Base pressure levels were determined as 40 %, 50 %, and 80 % (350, 455, and 750 MPa) of the value at which the test sample was fractured in the monotonic pressure profile. The experiments were performed according to the Taguchi L9 orthogonal experimental design given in Table 2.

To determine the bursting pressures at each parameter level, the samples were formed until fracturing at the forming depth of 13 mm with at least four repetitions. After the bursting pressures were determined, all the experiments were performed at 5 MPa below the bursting pressure. Thus, samples with at least three repetitions were obtained without any fracture. Fractured and unfractured samples are shown in Fig. 5. To calculate the R/t ratio, the nose radius was measured using the 3D optical scanning device. Both sides of the test samples were first lubricated with paraffin and covered with a polyethylene film.

Table 1
Chemical composition of the tested Ti-6Al-4V specimen.

Elements	Ti	Al	V	C	O	H	N	Fe
wt.%	89.72	6.08	4.05	0.010	0.069	0.0089	0.013	0.049

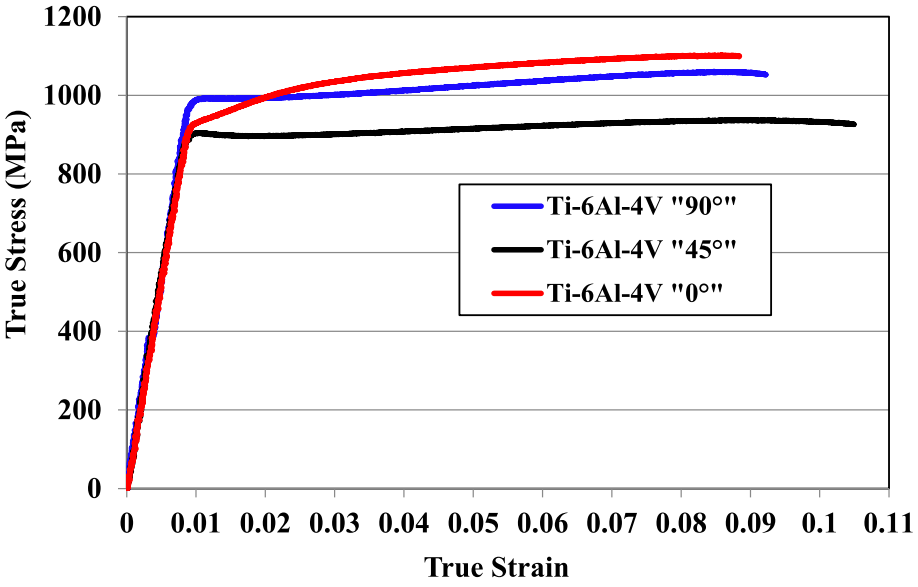

Fig. 1. The stress–strain curves for three rolling directions.

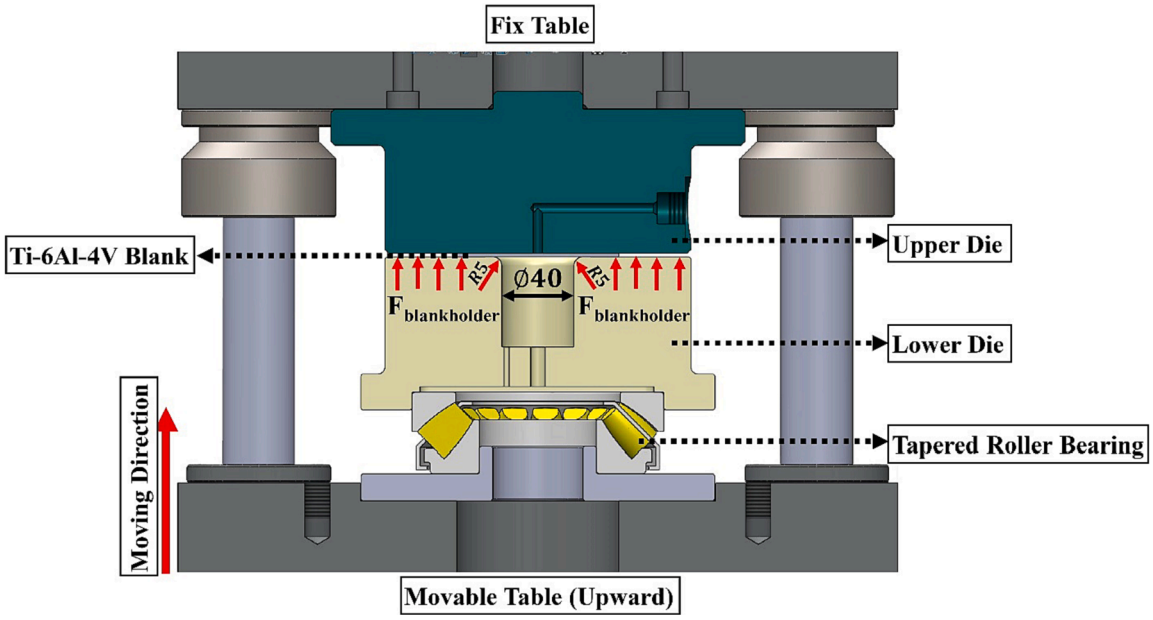

Fig. 2. The schematic representation of the experimental setup.

Material characterizations were performed on the samples obtained under the experimental conditions given in Table 3. The analyses, including XRD, FESEM, and TEM were performed following the standard metallographic processes. The regions from which the samples were prepared for the respective analyses are shown in Fig. 5. In the study conducted by Babu and Lindgren [21], it was stated that temperature affects the dislocation density and its mobility. Therefore, a waterjet was used to cut the required samples and to prevent excessive deformation and overheating during cutting.

The crystal structure and phases present in the microstructure of the samples were determined using the XRD analyses. A Rigaku X-ray diffractometer with Cu-Kα radiation (λ = 0.1542 nm) source was used operating at a voltage of 40 kV and a current of 20 mA. The diffraction scans were performed in the range of 30°-90°, while the scanning speed was set to 0.037°/s. Then, the observed XRD peaks were fitted by the Gaussian function, and a standard LaB6 sample was used to remove the instrumental broadening as a function of 2θ. Phase ratios in the microstructure were determined by calculating the area under the peaks. The Williamson-Hall plot was used to estimate the dislocation density after deducting the instrumental broadening as reported by Yang et al. [22]. ZEISS Gemini 500 FESEM was used to image the as-received microstructure and the fracture surfaces of the damaged specimens after

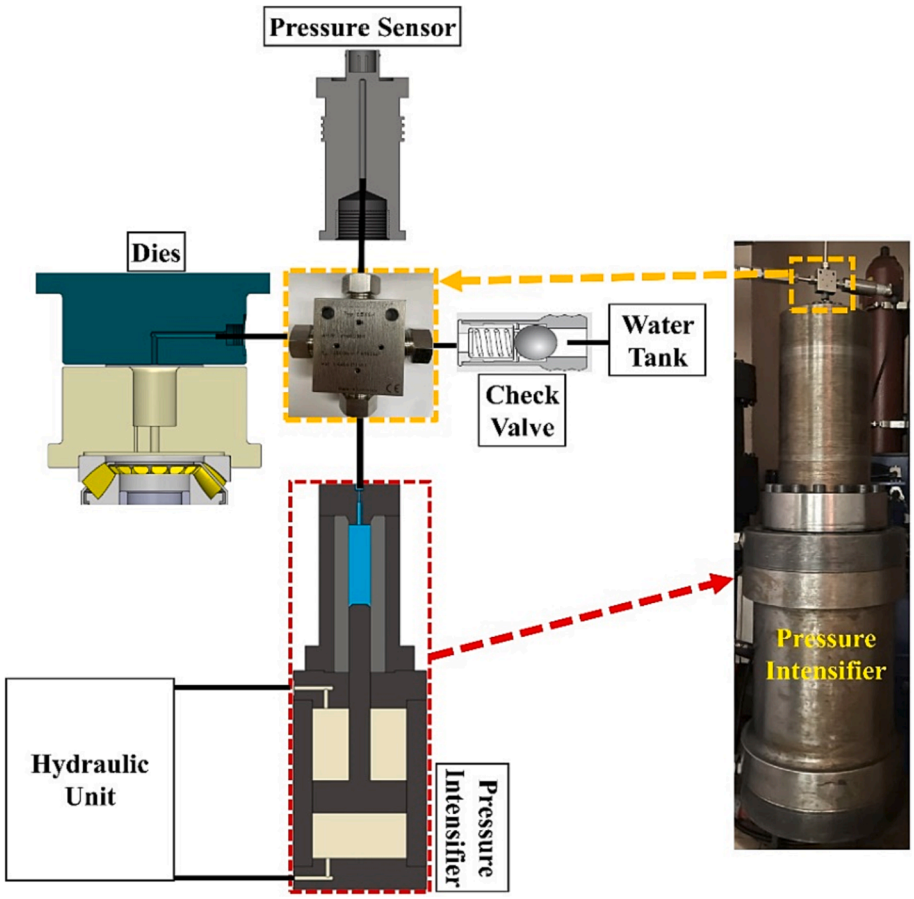

Fig. 3. The schematic representation of the hydraulic circuit.

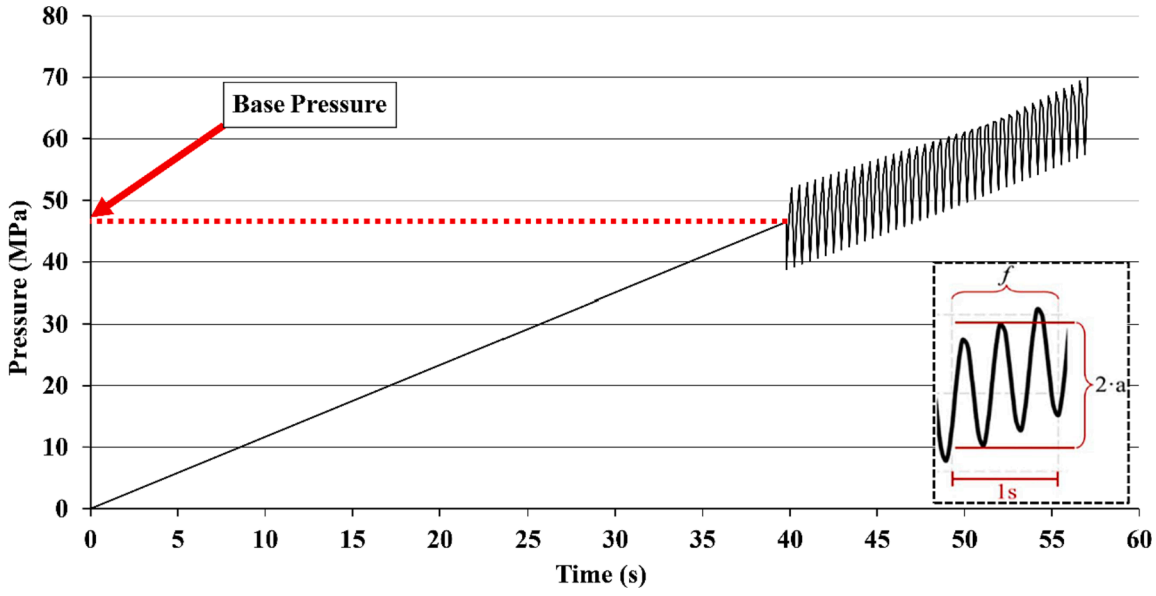

Fig. 4. An example pulsating loading profile (Ozturk et al., 2023).

monotonic and pulsating SHF-D processes. The detailed microstructural analyses of the samples were characterized by TEM using JEOL JEM-2100F, operating at 200 kV. Focused ion beam (FIB) microscopy was used to selectively prepare thin electron transparent specimens for TEM investigation using FEI-Nova 600i [23].

3. Finite element modelling of SHF-D

Finite Element Analyses (FEA) were conducted to select the suitable geometric parameters for the cylindrical cups formed using the SHF-D process. Within this scope, the cup diameter, depth, and forming pressure at which the cylindrical cup can be formed using the existing

Table 2
The design of experiments (Taguchi L9).

Exp. No.	Amplitude(MPa)	Frequency (Hz)	Base Pressure (MPa)
1	2.5	1	35.0
2	2.5	2	45.5
3	2.5	3	75.0
4	5.0	1	45.5
5	5.0	2	75.0
6	5.0	3	35.0
7	10.0	1	75.0
8	10.0	2	35.0
9	10.0	3	45.5

experimental press were identified. Additionally, the die shoulder (entrance) radius value was selected to ensure the flow without premature damage. FEA was conducted using the dynamic-explicit solver LS-DYNA. Initially, dies were modelled with 40 and 50 mm die inner diameters, 10, 13 and 15 mm die depths and 3, 4, and 5 mm die shoulder radii. Then a series of analyses were performed to determine the mesh independence point for a selected die geometry. Quad mesh sizes of 0.5, 0.75, 1, and 1.5 mm were used for the blank, and the analyses were executed. The thickness distribution graphs resulting from the analyses at 0°, 45°, and 90° angles are presented in Fig. 6, and the computation times are summarized in Table 4. Accordingly, it becomes evident that the analyses conducted with element sizes of 0.5 mm and 0.75 mm yield nearly identical values. Considering the computation times, it was deduced that employing quad elements with a size of 0.75 mm would be appropriate for the simulations, resulting in savings of approximately 11 h and 30 min per analysis.

The schematic representation of the simulation system is depicted in Fig. 7. The system, which was simplified according to the experimental setup, was modeled as a quarter model using shell elements and subjected to appropriate symmetry conditions. The lower die was completely fixed, while the upper die was constrained to move only along the z-axis. The pressure was defined as normal to the elements, to the region of the projection of the pressure area in the die on the sheet. In all finite element analyses and experiments, a fixed initial blank diameter of 72 mm was used. The dies of the SHF-D process are modeled as rigid. Since the workpiece to be formed in the experiments was lubricated, the friction coefficient between the lower die and the sheet and the upper die and the sheet was defined as 0.05 [24]. The Yoshida Uemori material model was used for the Ti-6Al-4V sheet [19]. The blank holder force (BHF) applied in the analysis was 50 kN. Mass scaling was also applied to reduce the dynamic effects in the explicit analysis. The rupture was controlled by the forming limit diagram obtained by the Nakazima test for 0.55 mm thick Ti-6Al-4V sheets (Fig. 8).

Table 3
The specimens for microstructural characterization.

No.	Loading Type	Damage Cond.	Pressure (MPa)
1	Monotonic	Damaged	90.3
2	Pulsating	Damaged	125.1
3	Pulsating	Damaged	120.1

4. Results and discussion

4.1. Finite element analysis

Initially, the cups with a smaller depth of 10 mm and a large inlet radius of 8 mm were formed without damage to verify the accuracy of the finite element analysis. Next, forming simulations of the same-sized cup were performed. The results obtained from the analyses were validated based on five different parameters: visual similarity, die entrance radius, nose radius, fluctuation distance in the edge regions and thickness distribution. As shown in Fig. 9a, there is a notable visual resemblance between the part formed using the SHF-D process and the part obtained from the analysis. For the second and third parameters, which are the entrance and nose radii, the values on the parts obtained from the analyses, as depicted in Fig. 9b, were measured from different regions using the LS-Prepost software. Similarly, radius measurements of the experimentally formed parts were made at different points by fitting cylinders tangent to the radius, as shown in Fig. 9c, using the Geomagic Control X software. The height of the fluctuations occurring in the edge regions after springback was measured in three different zones (Fig. 9d), both in the numerical and experimental analyses (Table 5). When the average values of these measurements were compared, the average deviation was found as 7.66 % for the entrance radius, 3.52 % for the nose radius, and 6.18 % for the fluctuation range. Moreover, in the simulations, the bursting pressure was predicted as 84 MPa until the sheet ruptures. In a series of repeated experiments conducted using the same parameters, ruptures occurred at an average pressure of 88.7 MPa. In this context, the bursting pressure was predicted with an accuracy of 95.7 %. When it was looked at the thickness distributions of the parts obtained experimentally and with FEA in Fig. 10, it is seen that FEA predicts the thickness distribution of the shaped part quite well.

Once the sufficiently accurate results were verified by the simulations, the appropriate geometric parameters were predicted by the simulation to obtain the cylindrical cups with higher depths and smaller radii. The results unveiled that the pressures reaching up to 150 MPa were needed to form the parts. The closing capacity of the experimental press was insufficient against the force generated by a pressure of 150 MPa at the surface of a 50 mm diameter die. Therefore, the maximum

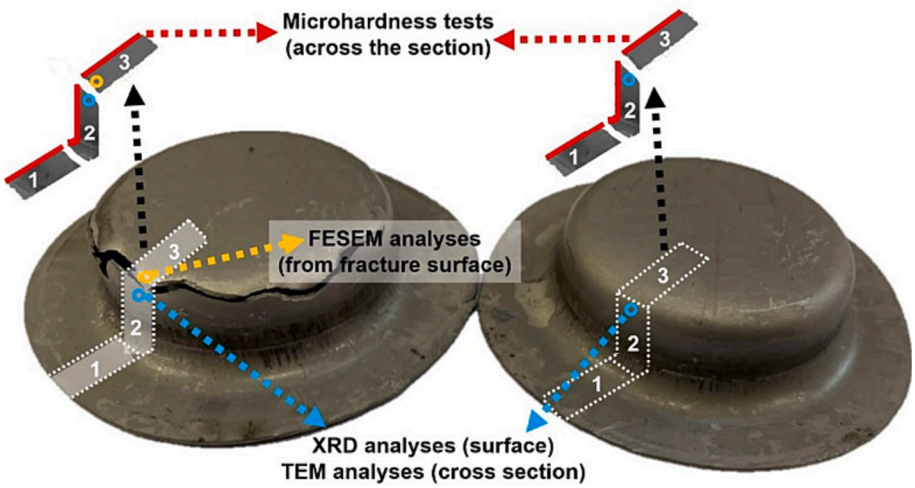

Fig. 5. Fractured and intact Ti-6Al-4V cups and the regions where samples are prepared for material characterizations.

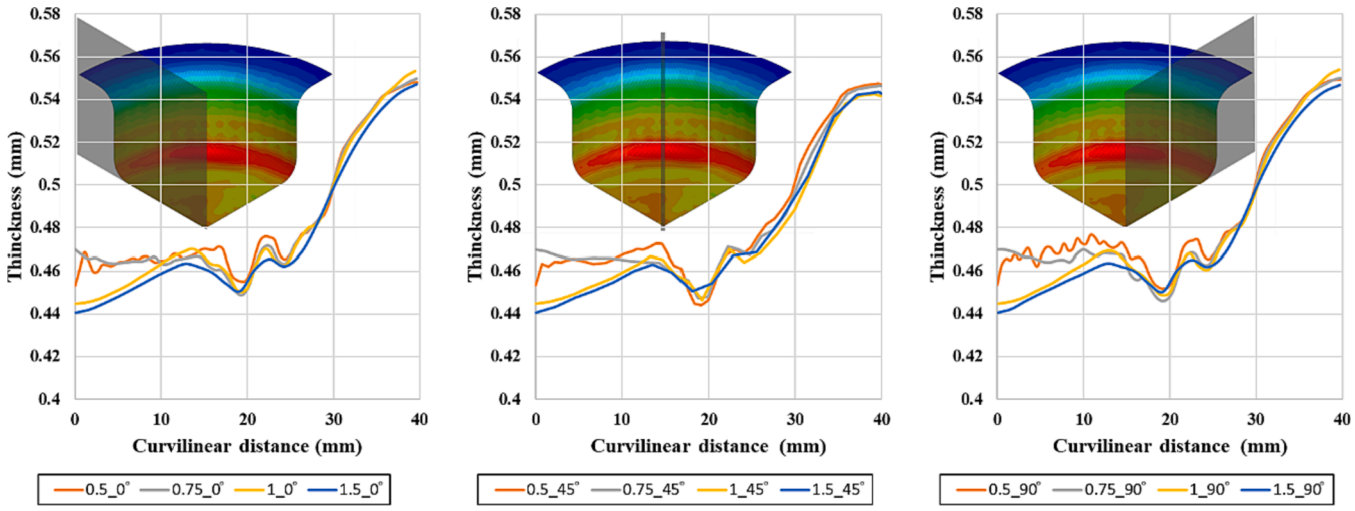

Fig. 6. Thickness variations predicted with various element sizes in 0°, 45° and 90° directions.

Table 4
The FE computation times for various element sizes.

Element Size	Computation Time
0.5	15 h 33 min 27 sec
0.75	3 h 56 min 5 sec
1	1 h 2 min 19 sec
1.5	0 h 33 min 57 sec

feasible die diameter used in the experiments was designed as 40 mm. Using the die with a diameter of 40 mm and a depth of 15 mm, parts with large nose radius could be obtained as shown in Fig. 11a. When the die height was 10 mm, a press capacity of 200 MPa was predicted and it exceeded the current capacity (Fig. 11b). Next, a die height of 13 mm was simulated, and it was predicted to be feasible for the currently available press (Fig. 11c). The optimal die entrance radius is the minimum value that would not cause premature failure by blanking. As seen in Fig. 11d, when the die entrance radius was 3 mm, the damage was predicted in this region. A 4 mm die entrance radius gave a marginal prediction (Fig. 11e); therefore, 5 mm was preferred with a lower risk of premature rupture (Fig. 11f).

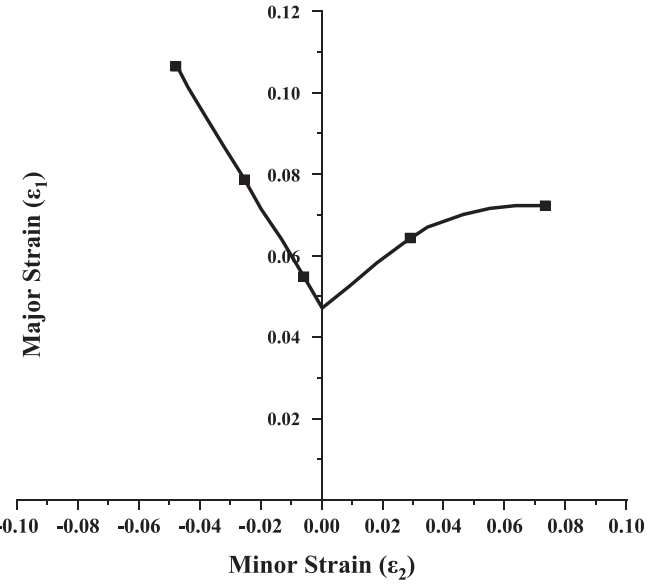

Fig. 8. Forming Limit Diagram of Ti-6Al-4V alloy sheet (thickness 0.5 mm).

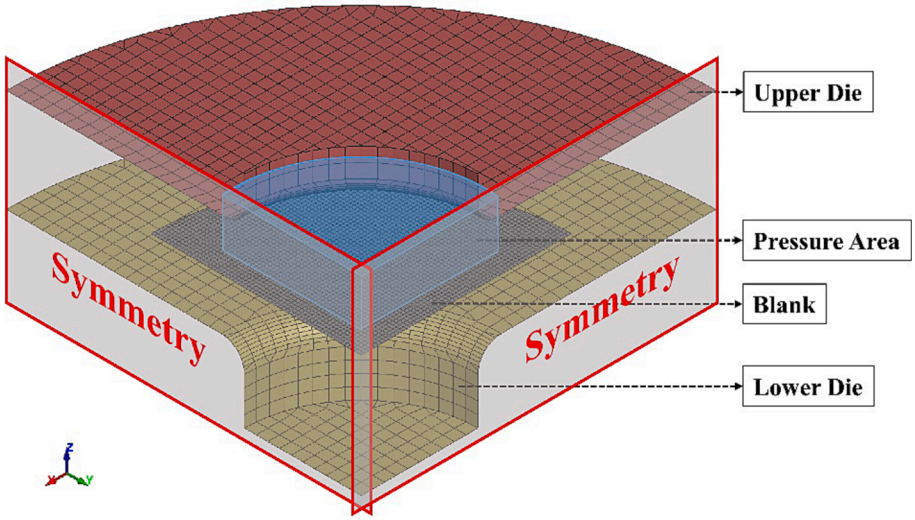

Fig. 7. The schematic representation of the finite element analysis system.

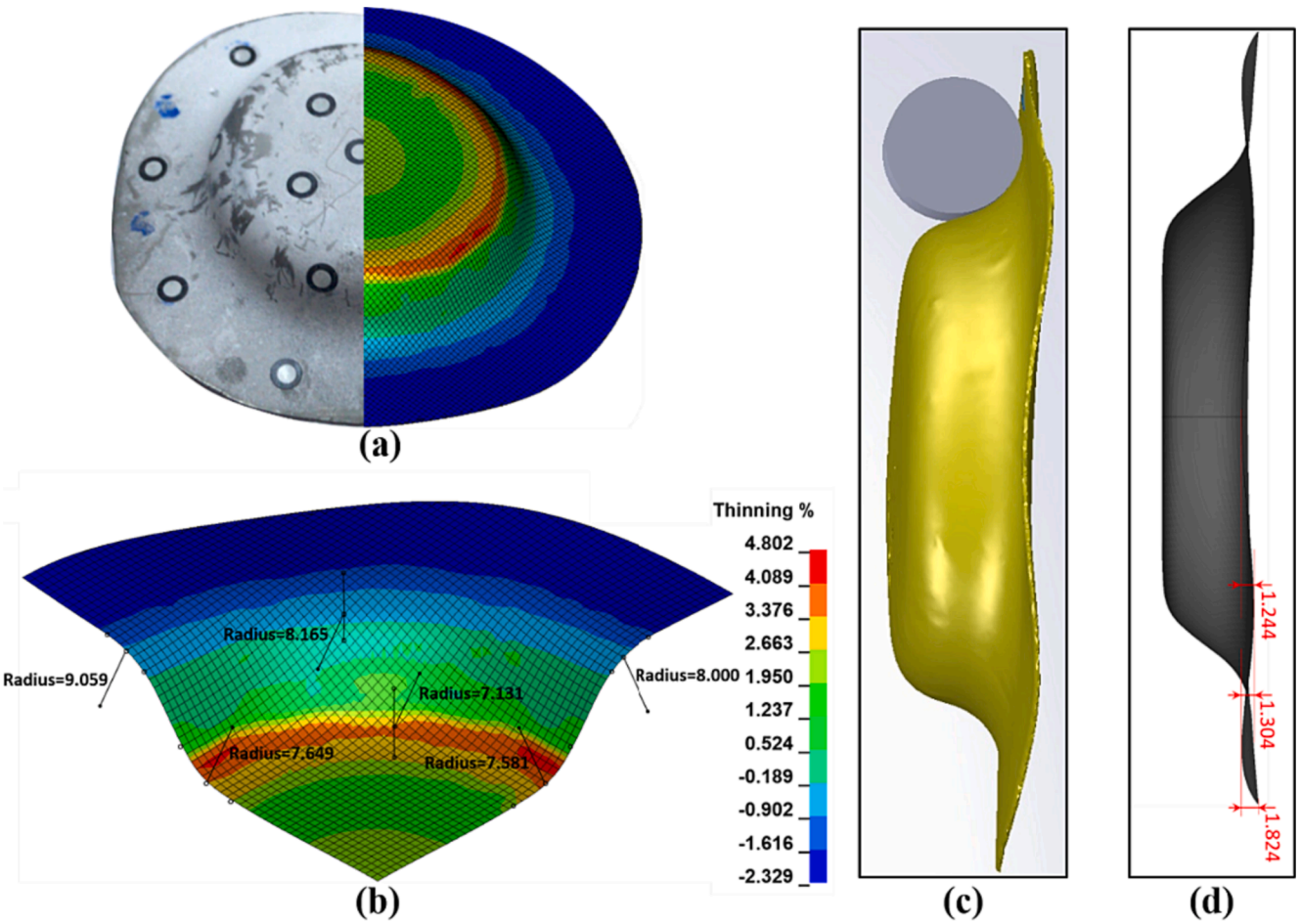

Fig. 9. (a) Parts obtained from FE analysis and the experiment (b) Entrance and nose radius measurements (c) Radius measurement from experimentally formed part (d) Measurement of wrinkling on the flange.

Table 5
Predicted and measured geometric results.

Validation Parameter	No	Predicted (mm)	Measured (mm)	Average Deviation Rate
Die Entrance Radius	1	9.059	8.222	7.66 %
	2	8.165	7.904	
	3	8.000	7.305	
	Avg.	**8.408 ± 0.570**	**7.810 ± 0.466**	
Nose Radius	1	7.649	7.44	3.52 %
	2	7.131	6.86	
	3	7.581	7.3	
	Avg.	**7.204 ± 0.281**	**7.200 ± 0.303**	
Wrinkling Period	1	1.744	0.99	6.18 %
	2	1.804	1.8	
	3	2.324	2.74	
	Avg.	**1.957 ± 0.319**	**1.843 ± 0.876**	

4.2. Forming process

The bursting pressures measured under the pulsating and monotonic loading are given in Table 6. The mean pressures at the burst were 90.4 and 93.7–118.8 MPa with monotonic regime and various pulsating loading conditions, respectively (Fig. 12). This shows an improvement of bursting pressure in the range of 3.8 % and 31.6 %.

One-way ANOVA is a statistical method used to test for significant differences between the means of three or more independent variables. If the p-value is less than the significance level (0.05), it can be concluded that there is a statistically significant difference between the means of the groups [25]. Thus, One-way ANOVA (analysis of variance) was performed to investigate whether there was a significant difference between the experimental repetitions. As seen in Table 7, the p-value was calculated less than 0.05 indicating a significant difference between the averages of the experimental results.

Fig. 13 shows the main effect plot of parameters on mean bursting pressure. No appreciable effect of amplitude and frequency on the bursting pressure was observed. However, with the increase of the base pressure, a significant increase in the bursting pressure was measured. When the initial pressure was set at 35.0, 45.0, and 75.0 MPa, the average rupture pressure was measured at 96.0, 94.0, and 103.5 MPa, respectively, indicating the influence of base pressure on the forming process.

The ANOVA results based on the bursting pressure are shown in Table 8. The p-values of the amplitude and frequency were higher than 0.05. Therefore, no significant effect of these parameters on bursting pressure was concluded. The p-value of the initial pressure was calculated as 0.062, which is marginally significant. Consequently, the base pressure has a 76.4 % effect on the bursting pressure with a total error ratio of 5.1 %.

The standard deviation of bursting pressures given in Table 6 was calculated as 5.0 MPa. Therefore, to obtain unfractured specimens, the blanks were formed at 5.0 MPa below the previously measured bursting pressure values. In the next phase, monotonic and pulsating hydroforming tests were repeated to form intact specimens to find the best combination of process parameters giving the sharpest nose radius. After the tests, all of the

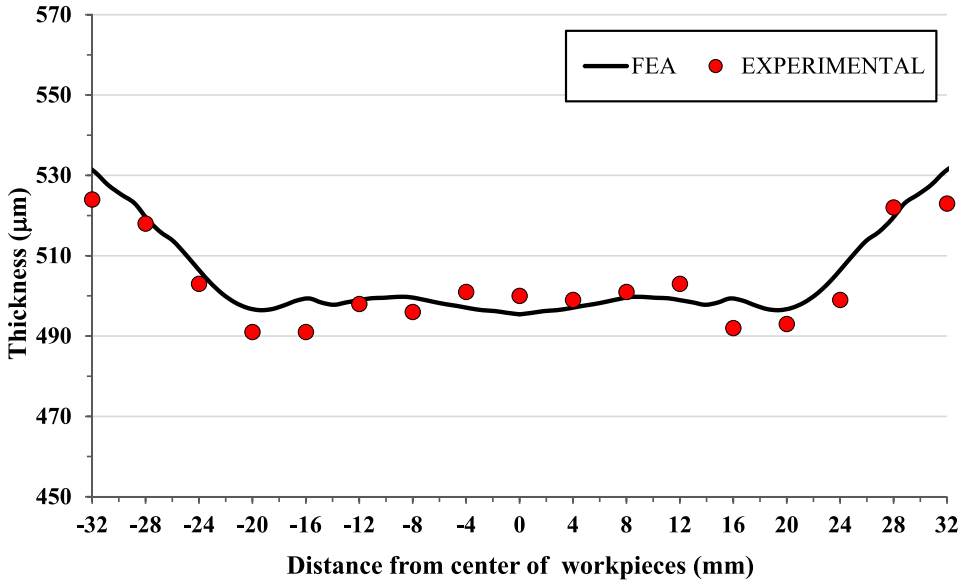

Fig. 10. Comparison of FEA results and experimental thickness distribution.

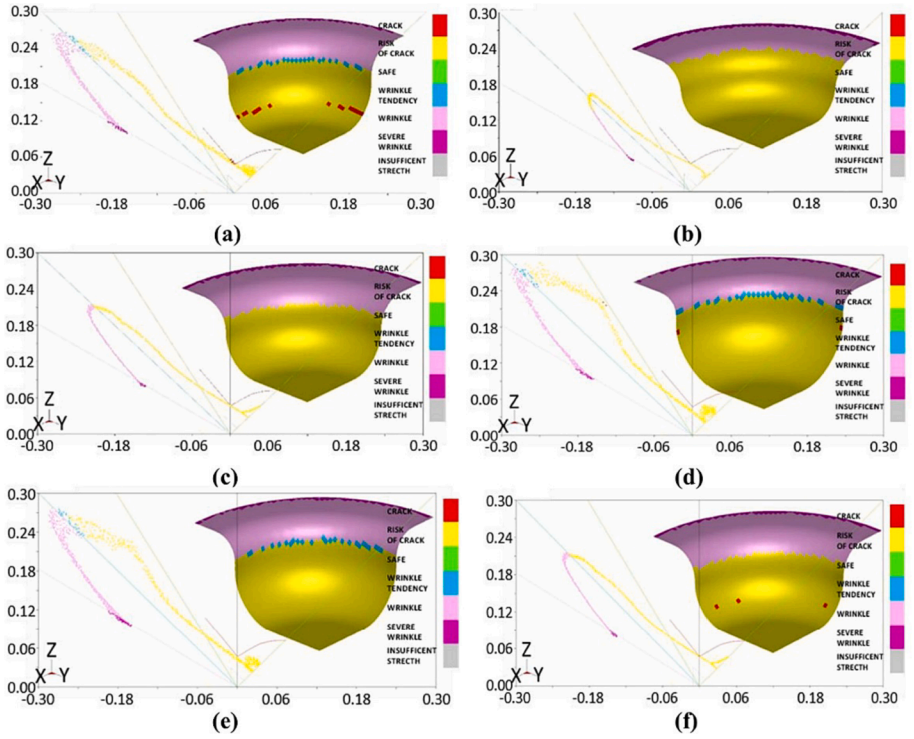

Fig. 11. Determination of die depth and entrance radius by FEA **(a)** Die diameter: 40 mm, depth: 15 mm. The part was damaged before it took the desired form **(b)** Die diameter: 40 mm, depth: 10 mm. Forming pressure exceeded press capacity **(c)** Die diameter: 40 mm, depth: 13 mm. The part where the forming pressure is suitable for the press capacity **(d)** Die diameter: 40 mm, entrance radius: 3 mm. Part damaged in entry radius area **(e)** Die diameter: 40 mm, entrance radius: 4 mm. The intact part close to damage **(f)** Die diameter: 40 mm, entrance radius: 5 mm. Undamaged part.

specimens were measured using a 3D optical scanner, and the R/t (nose radius/original sheet thickness) and die-filling ratios (specimen volume/die volume) were calculated. The measured nose radii and R/t ratios are cast in Table 9 and depicted in Fig. 14. Accordingly, the nose radii in all parts formed with pulsating loading were lower than the part formed under monotonic loading. Additionally, the smaller R/t ratio observed for the pulsating forming is an indication of the increased formability. The nose radii obtained by pulsating loading ranged between 6.48 mm and 8.73 mm, while it was 8.74 mm after monotonic loading. Parallel to the bursting pressure tests, the lowest nose radius was observed in Experiment 7 (10.0 MPa pulse amplitude, 1 Hz frequency, and 75.0 MPa base pressure). As a result, a notable improvement of 25.8 % was achieved in the R/t ratio by pulsating loading.

The other performance criterion that could be achieved by pulsating forming was the maximum thinning. In this context, the thickness distributions of the formed specimens under 9 pulsating and 1 monotonic loading conditions were measured and given in Fig. 15. Thickness measurements were made at 4 mm intervals. The center of the cylindrical cup was considered the “zero point”. The maximum thinning was measured as 8.3 % in Experiment-7. Consequently, further thinning of

Table 6
Bursting pressures under monotonic and pulsating loading.

Exp. No.	Amplitude (MPa)	Frequency (Hz)	Base Pressure (MPa)	1th Exp.	2th Exp.	3th Exp.	4th Exp.	5th Exp.	Mean Bursting Pressure (MPa)	Standard Deviation
1	2.5	1	35.0	99.7	101.0	95.2	96.0		98.0	2.8
2	2.5	2	45.5	90.5	98.7	92.5	98.5		95.1	4.2
3	2.5	3	75.0	110.0	96.5	91.3	108.5	85.4	101.6	10.7
4	5.0	1	45.5	94.8	87.9	90.0	85.0	113.1	94.2	11.2
5	5.0	2	75.0	98.3	100.6	99.0	98.5		99.1	1.0
6	5.0	3	35.0	92.6	96.1	97.3	93.4		94.9	2.2
7	10.0	1	75.0	140.0	95.6	116.5	119.0	122.7	118.8	11.6
8	10.0	2	35.0	96.7	94.8	95.4	92.4		94.8	1.8
9	10.0	3	45.5	102.2	92.0	90.5	90.0		93.7	5.7
Mon.	–	–	–	89.1	90.1	88.3	92.0	92.4	90.4	1.8

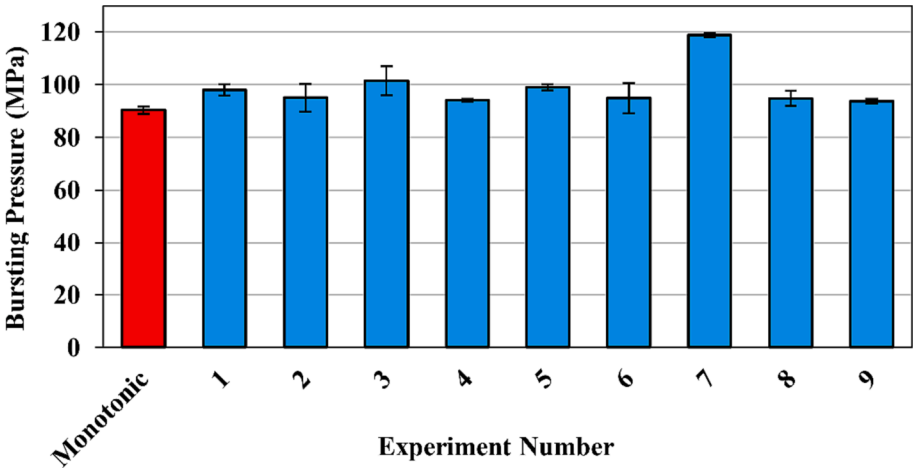

Fig. 12. The comparison of bursting pressures in monotonic and pulsating loading profiles.

Table 7
The one-way ANOVA results according to mean bursting pressure.

Source	Degree of freedom	Seq SS	Contribution (%)	Adj. MS	F-value	P-value
Parameters	9	159,248	55.7 %	17,694	4.62	0.001
Error	33	126,486	44.3 %	3833		
Total	42	285,734				

the material formed by pulsating without bursting is another indicator of the increased formability.

The Taguchi experimental design included a limited number of combinations. Yet, a set of optimized process parameters was found as 5.0 MPa pulse amplitude, 1 Hz pulse frequency, and 75.0 MPa base pressure. An additional experiment was performed by using optimized pulsating parameters and the bursting pressure was measured as 125.1 MPa, which is 38.5 % higher than the value under monotonic loading (Table 10). Besides, it is better than the optimum of bursting experiments, which was 31.6 %. The nose radius of the specimens formed with the optimized set of parameters was 6.1 mm, and the R/t ratio was calculated as 11.96 (Fig. 16) showing a remarkable improvement as compared to monotonic loading (Fig. 17).

Another performance criterion is the die-filling ratio. Since the tested geometry is a cylinder, a smaller cup nose radius indicates a better die-filling ratio. The volumes of the formed parts were measured using Geomagic Control X software and the results are listed in Table 11. The specimen formed under optimized pulsating parameters filled the die at a rate of 95.3 %. This ratio is quite high for a metal with such low formability compared to the literature. For example, Loh-Mousavi et al.

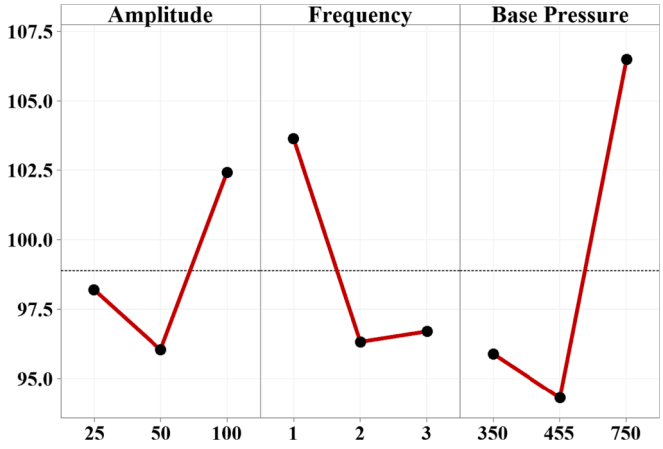

Fig. 13. The main effect plot of parameter levels on mean bursting pressure.

reached 80 % with mild steel under optimized parameters in pulsating tube hydroforming [14]. Koc et al. [26] reached 98.9 % die-filling with various types of stainless steel. Mohammadtabar et al. [27] attained 93.8 % for SS 304 in a double-step hydroforming process. 100 % die filling (with die with zero bottom radius) requires very high hydraulic pressures and a very ductile metal. Consequently, the improvement obtained on the Ti-6Al-4V sheet with pulsation is remarkable.

The last criterion is the homogeneity of the thickness distribution. That is, the lesser variation in the thickness strain indicates the more effective forming process. Accordingly, the measured thickness strains of the parts formed by the monotonic and optimized pulsating loading cases under the same maximum liquid pressure of 85.4 MPa were

Table 8
The ANOVA results of the mean bursting pressure.

Parameters	Degree of freedom	Seq SS	Contribution (%)	Adj. MS	F-value	P-value
Amplitude	2	2371	10.8 %	1185	2.13	0.319
Frequency	2	1700	7.7 %	850	1.53	0.395
Base P.	2	16,791	76.4 %	8395	15.10	0.062
Error	2	1112	5.1 %	556		
Total	8	21,973				

compared in Fig. 18. At the point where the maximum thickness strain was −4.7 % for monotonic loading, it was −2.8 % for optimized pulsating loading. That is, the specimen formed with pulsating loading had a much more homogeneous thickness distribution and the maximum thinning value was up to 40 % less.

4.3. Material characterization

Fig. 19 shows the XRD scans obtained before forming (as-received), after monotonic and pulsating forming indicating that both α and β phases are present in the microstructure of Ti-6Al-4V sheets. The calculations reveal the percentages of α and β phases as 96.9 % and 3.1 %, respectively, which is in line with the previously reported research [22]. The SEM image of the as-received sample is also given in Fig. 19 as an inset, revealing the typical microstructure of Ti-6Al-4V alloys. EDS analysis was performed for the composition analysis of phases showing different contrasts in the microstructure. As a result, two separate phases rich in vanadium and aluminum were detected. It is known that vanadium and aluminum elements stabilize β and α phases, respectively. Therefore, as a result of the composition analysis, the phases in the microstructure were named as shown in Fig. 19. The EDS analysis confirms that the microstructure consists of a dual-phase, that is, a majority of equiaxed α phase and a small portion of granular β phase along the grain boundaries.

The dislocation densities were estimated in the as-received sheet and the formed cylindrical cups and the results are given in Table 12. It should be borne in mind that these calculations give an estimate, rather than the exact value, to help interpret the results between the respective forming processes. Additionally, it is known that the dislocation motion that controls the plastic deformation of the material varies according to the crystal structures of the phases. Although the β phase (body-centered cubic structure) is more favorable in terms of deformation, the dominant effect is expected to come from the α phase during deformation since the α phase (hexagonal closed-packed structure) is larger in volume percentage [28]. Thus, the majority of plastic strain is assumed to be accommodated by the alpha phase, as suggested by Kulkarni et al. [29]. Accordingly, the change of the dislocation densities during monotonic and pulsating forming were compared for the α phase. As expected, the dislocation densities of formed specimens increased compared to the as-received (pre-forming) state of the material. That is, when the material was monotonically formed up to a tearing pressure of 90.3 MPa, the dislocation density increased from $2.07x10^{15}$ m^{-2} to $22.7x10^{15}$ m^{-2}. However, when the material was formed by pulsating loading to the same pressure without failure, the dislocation density was increased to $22.4x10^{15}$ m^{-2}. It should be noted that although both materials were formed up to 90.3 MPa pressures, dislocation density was found to be relatively lesser for the pulsating forming. However, when the material was formed up to a tearing pressure of 125.1 MPa with pulsating pressure, the dislocation density was increased to $24.6x10^{15}$ m^{-2}. That is,

Table 9
Nose radius/thickness ratios.

Exp. No.	Amplitude (MPa)	Frequency (Hz)	Base Pressure (MPa)	1th Exp.	2th Exp.	3th Exp.	4th Exp.	Mean Nose Radius (mm)	R/t (min)
1	2.5	1	35.0	8.39	8.02	8.56	8.54	8.38	17.8
2	2.5	2	45.5	8.33	8.65	9.09	8.69	8.69	17.9
3	2.5	3	75.0	8.87	8.51	8.39	8.42	8.55	17.4
4	5.0	1	45.5	8.48	9.06	8.65	8.73	8.73	17.4
5	5.0	2	75.0	8.02	7.76	8.26	8.01	8.01	16.9
6	5.0	3	35.0	8.29	8.89	9.01	8.55	8.68	17.7
7	10.0	1	75.0	6.56	6.42	6.46	6.48	6.48	13.9
8	10.0	2	35.0	8.39	8.38	8.60	8.38	8.44	17.6
9	10.0	3	45.5	8.38	8.37	8.65	8.09	8.37	17.8
Mon.	–	–	–	8.60	8.42	9.14	8.80	8.74	17.8

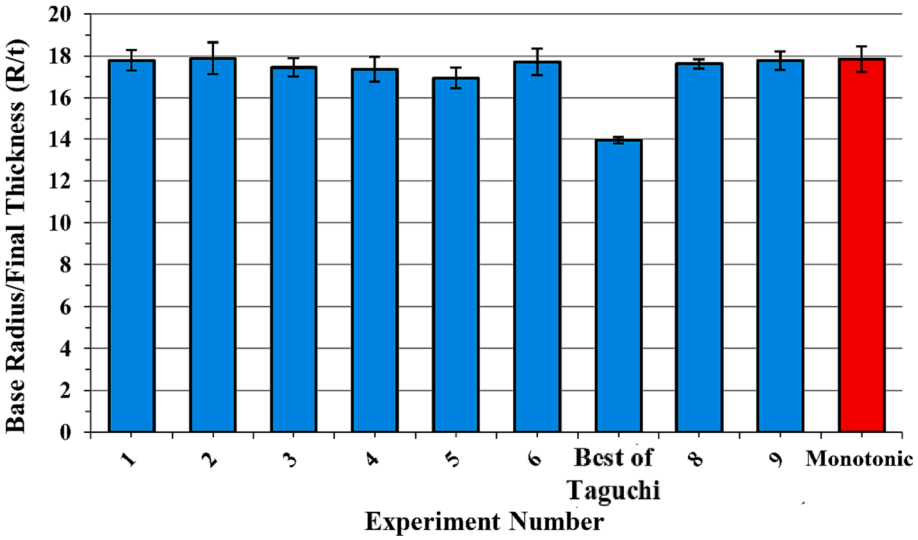

Fig. 14. The mean nose radius/thickness ratios attained by various experiments.

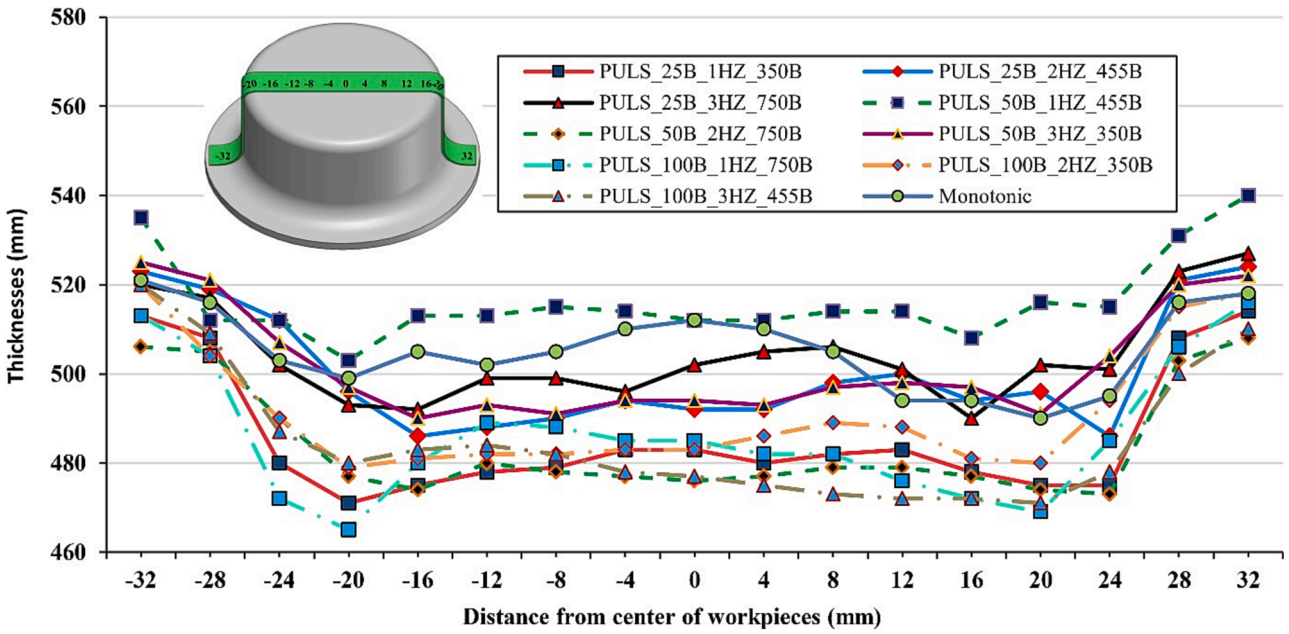

Fig. 15. Thickness variation of formed specimens with pulsating and monotonic loading.

Table 10
Bursting pressures for the pulsating, monotonic and optimized pulsating processes.

Exp.	Amplitude (MPa)	Frequency (Hz)	Base Pressure (MPa)	1st Exp.	2nd Exp.	3rd Exp.	4th Exp.	5th Exp.	Mean Bursting Pressure (MPa)	Standard Deviation
Best of Taguchi (7th exp.)	10.0	1	75.0	1400	956	1165	1190	1227	**118.8**	11.6
Monotonic	–	–	–	891	901	883	920	924	**90.4**	1.8
Optimum Pulsating	5.0	1	75.0	1095	1388	1223	1374	1176	**125.1**	12.3

stress relaxation occurred during pulsating forming allowing a higher deformation which caused the dislocation density to increase. Yamashita et al. [30] reported an approach stating that the stress is concentrated in a certain region during monotonic forming and eventually tearing occurs as the regions that reach high elastic deformation transform into plastic deformation locally. In pulsating forming, on the other hand, the regions that undergo plastic deformation are spread along the forming axes of the sample as a result of stress relaxation due to pressure increases and decreases, rather than being localized in a certain region. As a result, the tearing occurs later resulting in the formability improvement of the Ti-6Al-4V sheet at room temperature.

Detailed microstructural investigations of the formed parts via monotonic and pulsating fluid pressure were conducted. TEM images after the monotonic and pulsating formation are given in Fig. 20 with (a-c) and (d-f), respectively, from lower to higher magnifications. It is known that low-angle grain boundaries are dominant in cold-rolled samples [31], and can be a source of dislocation formation during plastic deformation [32]. In the current study, the as-received Ti-6Al-4V sheet was produced by cold rolling, and accordingly, various types of dislocations were observed in the microstructures, including mixed dislocations, dislocation walls, dislocation cells and dislocation complexes. Upon comparing the monotonically formed sample, as depicted in Fig. 20 (a-c), to the pulsating-formed sample, as depicted in Fig. 20 (d-f), it was observed that the dislocation density is relatively lower in coarser grains of the monotonic-formed sample. On the other hand, a higher dislocation density as well as sub-grains and dislocation cells is evident in the pulsating-formed sample. The reason for this is the increased formability in the case of pulsating pressure, the formation of new dislocations, and the increase in dislocation density due to additional plastic deformation, which reaches a higher die-filling ratio in the SHF-D processes. However, if the samples were formed monotonically and with pulsation at the same deformation ratio, lower dislocation density would be observed in the TEM images due to the effect of stress relaxation, as stated by Mohebbi et al. [33]. Also, as can be seen in Fig. 20b and Fig. 20e, dislocation pile-ups occurred in both monotonic and pulsating forms. It is known that dislocation pile-ups at the

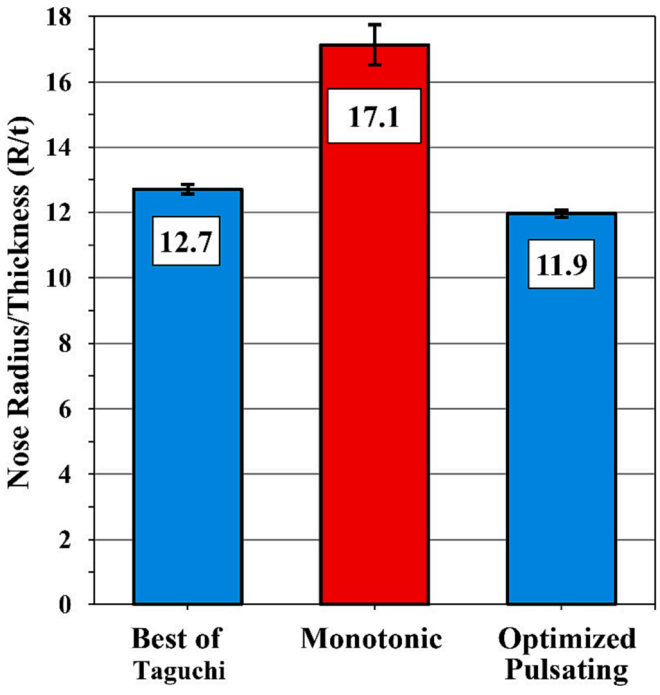

Fig. 16. The mean nose radius/thickness ratios for pulsating, monotonic and optimized pulsating processes.

Fig. 17. The specimens formed by (a) monotonic and (b) optimized pulsating process.

Table 11
Die-filling ratios for pulsating, monotonic and optimized pulsating processes.

Exp. No.	1st Exp. (mm^3)	2nd Exp. (mm^3)	3rd Exp. (mm^3)	4rt Exp. (mm^3)	Mean Volume (mm^3)	Die Volume (mm^3)	Workpiece/ Die	Std. Dev.	Volumetric Improvement (%)
1	14,323	13,614	14,111	14,110	14,040	15,664	89.6	300.8	1.9
2	13,642	14,196	13,966	–	13,935	15,664	89.0	278.3	1.2
3	14,312	14,036	13,618	14,207	14,043	15,664	89.7	305.5	2.0
4	14,123	14,142	13,780	–	14,015	15,664	89.5	203.7	1.8
5	14,564	14,425	14,110	–	14,366	15,664	91.7	232.6	4.2
6	14,169	14,255	14,236	14,262	14,231	15,664	90.8	42.4	3.3
7	14,572	14,857	14,529	–	14,653	15,664	93.5	178.3	6.0
8	14,206	14,237	14,211	14,422	14,269	15,664	91.1	102.9	3.5
9	13,767	13,726	13,916	13,728	13,784	15,664	88.0	89.8	0.1
OPT_PULS	14,992	14,974	14,808	14,925	14,925	15,664	95.3	101.4	7.8
Monotonic	13,853	13,586	13,816	13,815	13,768	15,664	87.9	122.3	–

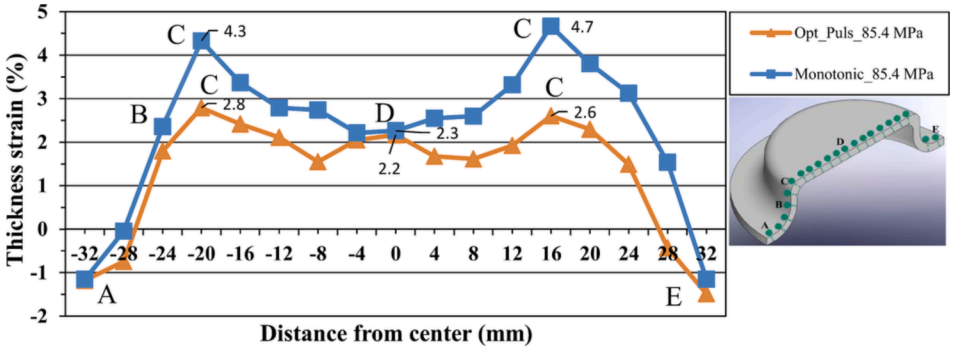

Fig. 18. Thickness strain variation of formed specimens with pulsating and monotonic loading.

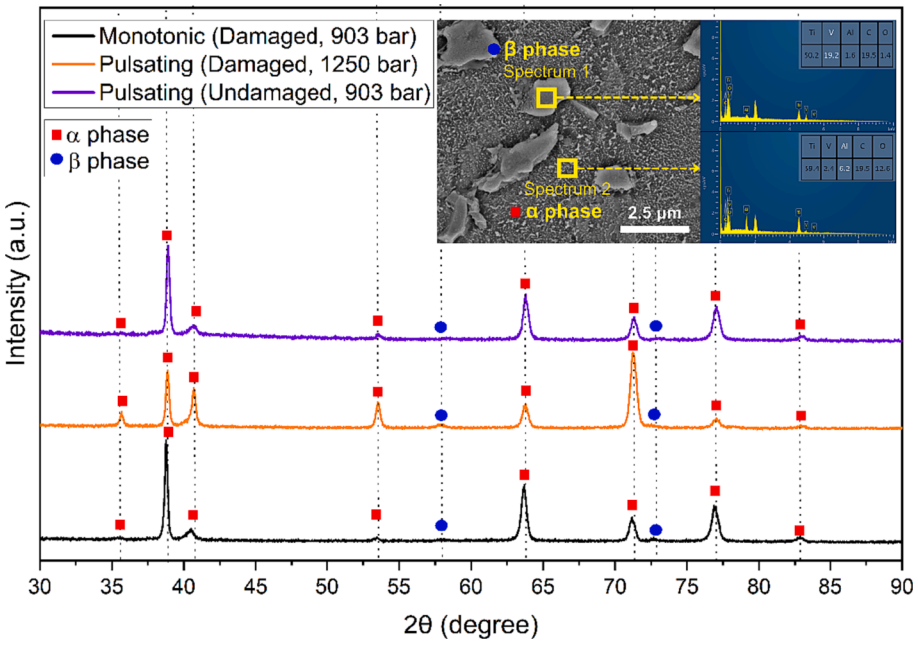

Fig. 19. The XRD scans of formed specimens and the microstructure of the as-received Ti-6Al-4V sheet.

Table 12
The dislocation density values, and phase ratios obtained from XRD analysis of the formed specimens.

Num.	Workpiece	Dislocation Density x10^{15} m^{-2}		Phase Ratio (%)	
		Alfa	Beta	Alfa	Beta
1	Monotonic Loading (Damaged. 90.3 MPa)	22.7	14.9	97.7	2.3
2	Pulsating (Damaged. 125.1 MPa)	24.6	51	96.8	3.2
3	Pulsating (Undamaged. 90.3 MPa)	22.4	11.1	97.6	2.4
4	Pre-forming (As-received)	2.07	2.02	96.9	3.1

interfaces between the α and β phases occur due to an inconsistency in the slip planes between the two phases and these pile-ups lead to the deformation band in the α phase [34]. Therefore, the majority of plastic strain is assumed to be accommodated by the α phase, as suggested by Kapoor et al. [28]. Consequently, the TEM images confirmed the dislocation densities calculated from the XRD results.

The fracture surfaces of Ti-6Al-4V alloy after (a) monotonic and (b) pulsating-forming are given in Fig. 21. The regions indicated by the dashed lines in each micrograph give a magnified view of the same region. It can be observed from the figure that the monotonically formed part consists of a bright damaged surface showing mostly brittle fracture characteristics. This is due to the nature of the low plastic deformation observed in Ti-6Al-4V alloy. It has been reported in the literature that Ti-6Al-4V alloy exhibits an abrupt fracture during tensile testing without significant necking [35]. However, when the material is formed with pulsating loading, besides the surfaces showing brittle-like fracture, dimples are also seen on the damaged surface, indicating that relatively more plastic deformation occurs due to the stress relaxation as a result of pulsation (Fig. 21b). It has been explained in the literature that the nucleation of new voids before fracture is predominant in materials with higher deformation ability [36,37]. In monotonic forming, on the other hand, it is relatively more brittle, that is, fracture occurs earlier as a result of the growth and coalescence of dimples before new voids can nucleate [38].

5. Conclusions

Previously, the effect of pressure pulsation on the formability of sheet Ti–6Al–4V was investigated on the pulsating hydraulic bulge test [19,20]. In the current study, the effect of pulsation was tested on a

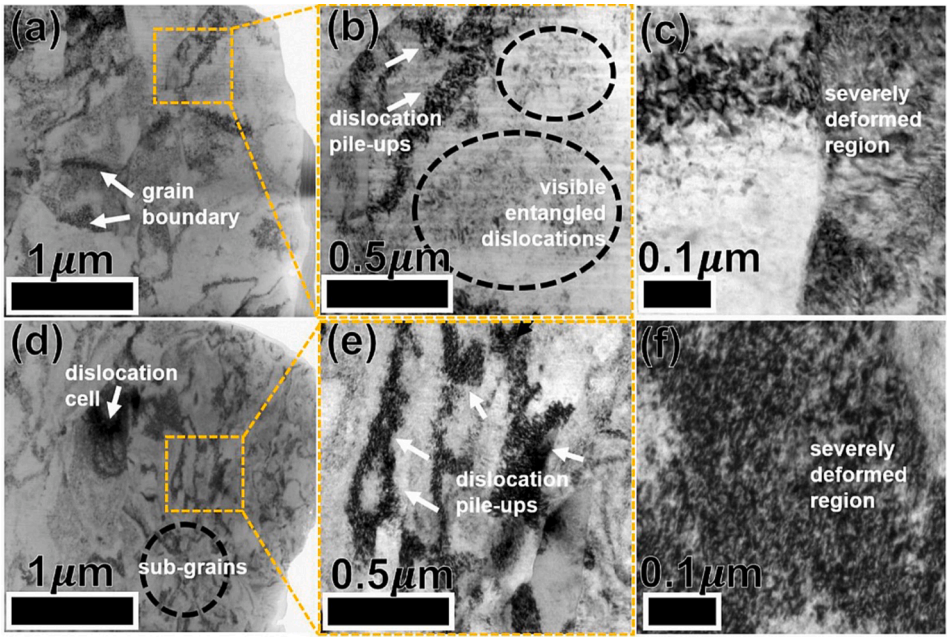

Fig. 20. TEM images after the monotonic and pulsating forming are given with (a-c) and (d-f), respectively.

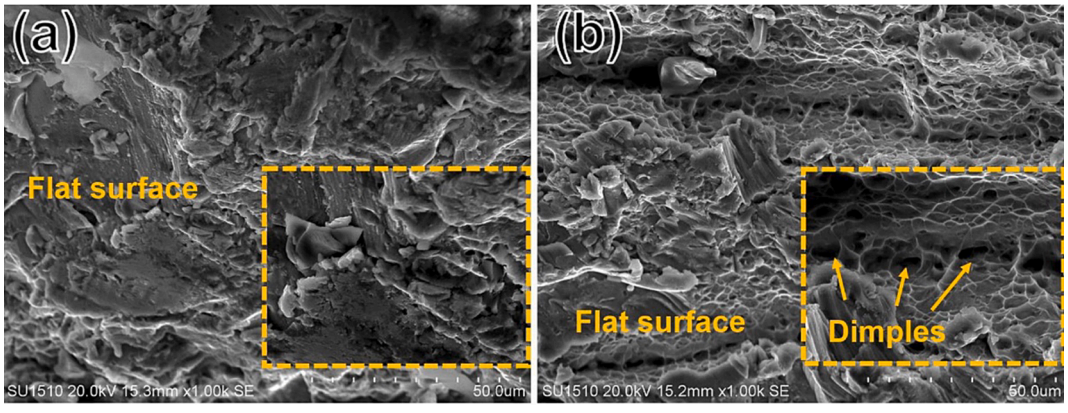

Fig. 21. Fracture surface fractographs (a) Monotonic loading (b) Pulsating loading.

small-scale cylindrical cup of the same material in the SHF-D process, where friction is effective, unlike the hydraulic bulge test. A set of tests followed by microstructural investigations were conducted to verify the formability improvement due to pulsation under frictional conditions valid in the industrial processes. Some concluding remarks are as follows.

- The burst pressure under pulsating loading increased from 90.3 to 125.1 MPa as compared to the monotonic one.
- The ANOVA showed that the base pressure was the most effective parameter on the burst pressure by 76.4 %. The best performance was obtained at 5.0 MPa pulse amplitude and 1 Hz frequency under 75.0 MPa base pressure.
- The average nose radius was reduced from 8.74 to 6.1 mm by pulsating loading. That is the R/t ratio reduced from 17.1 to 11.9, a 30.4 % improvement.
- The maximum thickness reduction at the fracture occurred at 8.3 % instead of 4.9 % with a remarkably more homogeneous thickness distribution with pulsating loading.
- The fracture surface analysis of the specimens formed by pulsating loading showed that there were regions on the damaged cross-section with characteristic dimple-like features indicating that more plastic deformation occurred during the pulsating forming.
- When the effect of pulsating loading is compared over the thickness strain values where the fracture occurs, the thickness strain doubled in the free bulging condition (Yapan et al., 2023), while it increased 1.7 times in the SHF-D process. So, it is thought that friction somewhat suppresses the enhancement of pulsation on material fracture

Declaration of competing interest

The authors declare the following financial interests/personal relationships which may be considered as potential competing interests: Mevlut Turkoz reports financial support was provided by THE SCIENTIFIC AND TECHNOLOGICAL RESEARCH COUNCIL OF TÜRKİYE.

Acknowledgements

This work was supported by the Scientific and Technological Research Council of Türkiye (TUBITAK) [grant number 219M489].

References

[1] M. Paghandeh, A. Zarei-Hanzaki, H.R. Abedi, Y. Vahidshad, On the warm temperature strain accommodation mechanisms of Ti-6Al-4V alloy holding different starting microstructures, J. Mater. Res. Technol. 14 (2021) 496–506, https://doi.org/10.1016/j.jmrt.2021.06.077.
[2] M. Paghandeh, A. Zarei-Hanzaki, H.R. Abedi, Y. Vahidshad, P. Minarik, The correlation of c-to-a axial ratio and slip activity of martensite including microstructures during thermomechanical processing of Ti–6Al–4V alloy, J. Mater. Res. Technol. 18 (2022) 577–583, https://doi.org/10.1016/j.jmrt.2022.02.105.
[3] C. De Formanoir, A. Brulard, S. Vivès, G. Martin, F. Prima, S. Michotte, S. Godet, A strategy to improve the work-hardening behavior of Ti–6Al–4V parts produced by additive manufacturing, Materials Research Letters 5 (3) (2017) 201–208.
[4] Y.G. Ko, W.G. Kim, C.S. Lee, D.H. Shin, Microstructural influence on low-temperature superplasticity of ultrafine-grained Ti–6Al–4V alloy, Mater. Sci. Eng. A 410 (2005) 156–159, https://doi.org/10.1016/j.msea.2005.08.080.
[5] H.L. Du, P.K. Datta, D.B. Lewis, J.S. Burnell-Gray, Air oxidation behaviour of Ti-6Al-4V alloy between 650 and 850, Corros. Sci. 36 (4) (1994) 631–642, https://doi.org/10.1016/0010-938X(94)90069-8.
[6] H.J. Bong, D.H. Yoo, D. Kim, Y.N. Kwon, J. Lee, Correlative study on plastic response and formability of Ti-6Al-4V sheets under hot forming conditions, J. Manuf. Process. 58 (2020) 775–786, https://doi.org/10.1016/j.jmapro.2020.08.053.
[7] C. Bell, J. Corney, N. Zuelli, D. Savings, A state of the art review of hydroforming technology: Its applications, research areas, history, and future in manufacturing, Int. J. Mater. Form. 13 (2020) 789–828, https://doi.org/10.1007/s12289-019-01507-1.
[8] M. Bakhshi-Jooybari, A. Gorji, M. Elyasi, Developments in sheet hydroforming for complex industrial parts, Met. Form. 3 (2012) 55–84, https://doi.org/10.5772/48142.
[9] M.S. Ankaralı, M. Dilmeç, M. Türköz, Investigation on the effect of use of movable die in sheet hydroforming with die on formability, J. Fac. Eng. Archit. Gaz. 35 (2) (2020) 787–801. 10.17341/gazimmfd.521754.
[10] E. Önder, A.E. Tekkaya, Numerical simulation of various cross-sectional specimens using conventional deep drawing and hydroforming technologies, Int J Mach Tool Manu 48 (5) (2008) 532–542, https://doi.org/10.1016/j.ijmachtools.2007.06.012.
[11] M. Dilmeç, V. Bülüç, Determination of limit drawing ratio of SS 304 steel using sheet hydroforming process with female die, Indian J. Eng. Mater. Sci. 29 (5) (2022) 649–657. 10.56042/ijems.v29i5.49043.
[12] K. Mori, A.U. Patwari, S. Maki, Improvement of formability by oscillation of internal pressure in pulsating hydroforming of tube, CIRP Ann. 53 (1) (2004) 215–218, https://doi.org/10.1016/S0007-8506(07)60682-9.
[13] T. Hama, M. Asakawa, H. Fukiharu, A. Makinouchi, Simulation of hammering hydroforming by static explicit FEM, ISIJ Int. 44 (1) (2004) 123–128, https://doi.org/10.2355/isijinternational.44.123.
[14] M. Loh-Mousavi, K. Mori, K. Hayashi, S. Maki, M. Bakhshi, 3-D finite element simulation of pulsating T-shape hydroforming of tubes, Key Eng. Mater. 340 (2007) 353–358, https://doi.org/10.4028/www.scientific.net/KEM.340- 341.353.
[15] A. Mostafapour, A. Akbari, M.R. Nakhaei, Application of response surface methodology for optimization of pulsating blank holder parameters in deep drawing process of Al 1050 rectangular parts, Int. J. Adv. Manuf. Technol. 91 (2017) 731–737, https://doi.org/10.1007/s00170-016-9781-z.
[16] C. Shi, A. Wang, J. Li, Study on pulsating hydroforming of equal wall thickness spiral tube for shale gas exploitation, Int. J. Adv. Manuf. Technol. 120 (5) (2022) 4217–4231, https://doi.org/10.1007/s00170-022-08913-x.
[17] L.F. Yang, L. Yi, C. Guo, Influence of pressure amplitude on formability in pulsating hydro-bulging of AZ31B magnesium alloy sheet, Appl. Mech. Mater. 128 (2012) 397–402, https://doi.org/10.4028/www.scientific.net/AMM.128-129.397.
[18] G. Hu, C. Pan, Investigation on deformation behavior of magnesium alloy sheet AZ31B in pulsating hydroforming, Proc. Inst. Mech. Eng. Part B: J. Eng. Manuf. 235 (1–2) (2021) 198–206. 10.1177/0954405420947950.
[19] O. Öztürk, et al., Formability improvement in Ti–6Al–4V sheet at room temperature by pulsating hydraulic bulging: experimental and numerical investigations, Int. J. Adv. Manuf. Technol. 124 (7–8) (2023) 2903–2918, https://doi.org/10.1007/s00170-022-10693-3.
[20] Y.F. Yapan, et al., Microstructural characterization of improved formability of Ti-6Al-4V sheet by pulsating hydraulic bulging at room temperature, J. Mater. Eng. Perform. 32 (2023) 6258–6269, https://doi.org/10.1007/s11665-022-07550-5.
[21] B. Babu, L.E. Lindgren, Dislocation density based model for plastic deformation and globularization of Ti-6Al-4V, Int. J. Plast 50 (2013) 94–108, https://doi.org/10.1016/j.ijplas.2013.04.003.
[22] J. Yang, J. Wu, Q. Zhang, R. Han, K. Wang, Investigation of flow behavior and microstructure of Ti–6Al–4V with annealing treatment during superplastic forming, Mater. Sci. Eng. A (2020) 797, https://doi.org/10.1016/j.msea.2020.140046.
[23] H. Kotan, Thermal stability, phase transformation and hardness of mechanically alloyed nanocrystalline Fe-18Cr-8Ni stainless steel with Zr and Y2O3 additions, J. Alloy. Compd. 749 (2018) 948–954, https://doi.org/10.1016/j.jallcom.2018.03.324.
[24] M. Türköz, Ö.N. Cora, H. Gedikli, M. Dilmeç, H.S. Halkacı, M. Koc, Numerical optimization of warm hydromechanical deep drawing process parameters and its experimental verification, J. Manuf. Process. 57 (2020) 344–353, https://doi.org/10.1016/j.jmapro.2020.06.020.
[25] P.H. Westfall, K.S. Henning, Understanding advanced statistical methods, CRC, Boca Raton, 2013.
[26] M. Koç, S. Mahabunphachai, E. Billur, Forming characteristics of austenitic stainless steel sheet alloys under warm hydroforming conditions, Int. J. Adv. Manuf. Technol. 56 (2011) 97–113, https://doi.org/10.1007/s00170-011-3169-x.
[27] N. Mohammadtabar, M. Bakhshi-Jooybari, S.J. Hosseinipour, A.H. Gorji, Feasibility study of a double-step hydroforming process for fabrication of fuel cell bipolar plates with slotted interdigitated serpentine flow field, Int. J. Adv. Manuf. Technol. 85 (2016) 765–777, https://doi.org/10.1007/s00170-015-7960-y.
[28] K. Kapoor, P. Ravi, R. Noraas, J.S. Park, V. Venkatesh, M.D. Sangid, Modeling Ti–6Al–4V using crystal plasticity, calibrated with multi-scale experiments, to understand the effect of the orientation and morphology of the α and β phases on time-dependent cyclic loading, J. Mech. Phys. Solids 146 (2021) 104192, https://doi.org/10.1016/j.jmps.2020.104192.
[29] G. Kulkarni, V. Hiwarkar, J. Patil, R. Singh, Microstructural Behavior of Ti6Al4V during Room Temperature Deformation, J. Nanosci. Nanotechnol. Res. 2 (1) (2018) 1–4.
[30] H. Yamashita, H. Ueno, H. Nakai, T. Higaki, Technology to enhance deep-drawability by strain dispersion using stress relaxation phenomenon, SAE Int. (2015), https://doi.org/10.4271/2015-01-0531.
[31] C. Jiang, Q. Gao, H. Zhang, Z. Liu, H. Li, Microstructure and Mechanical Properties of 4Al Alumina-Forming Austenitic Steel after Cold-Rolling Deformation and Annealing, Materials (basel) 13 (12) (2020) 2767, https://doi.org/10.3390/ma13122767.
[32] J. Charkhchian, A. Zarei-Hanzaki, A. Moshiri, H.R. Abedi, T.M. Schwarz, R. Lawitzki, G. Schmitz, K. Chadha, C. Aranas, J. Shen, J.P. Oliveira, Spinodal Decomposition of B2-phase and Formation of Cr-Rich Nano-precipitates in AlCoCrFeNi2.1 Eutectic High-Entropy Alloy, Adv. Eng. Mater. 25 (2023) 2300164, https://doi.org/10.1002/adem.202300164.
[33] M.S. Mohebbi, A. Akbarzadeh, Y.O. Yoon, S.K. Kim, Stress relaxation and flow behavior of ultrafine-grained AA 1050, Mech. Mater. 89 (2015) 23–34, https://doi.org/10.1016/j.mechmat.2015.06.001.

[34] Y. Zhang, D. Li, X. Li, X. Liu, S. Zhao, Y. Li, Creep deformation and strength evolution mechanisms of a Ti-6Al-4V alloy during stress relaxation at elevated temperatures from elastic to plastic loading, J. Mater. Sci. Technol. 126 (2022) 93–105, https://doi.org/10.1016/j.jmst.2022.02.042.
[35] O.M. Badr, B. Rolfe, P. Hodgson, M. Weiss, Forming of high-strength titanium sheet at room temperature, Mater. Des. 66 (2015) 618–626, https://doi.org/10.1016/j.matdes.2014.03.008.
[36] B. Valoppi, S. Bruschi, A. Ghiotti, Modelling of fracture onset in Ti6Al4V sheets deformed at elevated temperature, Procedia Manuf. 5 (2016) 248–258, https://doi.org/10.1016/j.promfg.2016.08.022.
[37] P. Verleysen, J. Peirs, Quasi-static and high strain rate fracture behaviour of Ti6Al4V, Int. J. Impact Eng 108 (2017) 370–388, https://doi.org/10.1016/j.ijimpeng.2017.03.001.
[38] M. Giglio, A. Manes, F. Vigano, Ductile fracture locus of Ti–6Al–4V titanium alloy, Int. J. Mech. Sci. 54 (2012) 121–135, https://doi.org/10.1016/j.ijmecsci.2011.10.003.